Materials Science & Engineering A 814 (2021) 141194

Contents lists available at ScienceDirect

Materials Science & Engineering A

journal homepage: http://www.elsevier.com/locate/msea

Effect of deposition strategies on fatigue crack growth behaviour of wire + arc additive manufactured titanium alloy Ti–6Al–4V

Abdul Khadar Syed [a,*], Xiang Zhang [a,**], Alec E. Davis [b], Jacob R. Kennedy [b], Filomeno Martina [c], Jialuo Ding [c], Stewart Williams [c], Philip B. Prangnell [b]

[a] Faculty of Engineering, Environment and Computing, Coventry University, CV1 5FB, UK
[b] Department of Materials, University of Manchester, M13 9PL, UK
[c] Welding Engineering and Laser Processing Centre, Cranfield University, MK43 0AL, UK

ARTICLE INFO

Keywords:
Additive manufacturing
WAAM
Fatigue crack growth rate
Crack deflection
Titanium alloys

ABSTRACT

The influence of three deposition strategies on the fatigue crack growth behaviour of Wire + Arc Additive Manufactured (WAAM) Ti–6Al–4V has been investigated in the as-built condition. Test samples were prepared using single pass, parallel pass, and oscillation deposition strategies and tested with cracks propagating parallel and normal to the plane of deposition. Due to the higher local heat input, the oscillation build exhibited a significantly coarser columnar β grain structure as well as a coarser transformation microstructure, compared to the single pass and parallel pass builds, which were very similar. Among the three build methods, the lowest crack growth rates were found with the oscillation build. The crack growth data was found to broadly fall between that of a recrystallized α (mill-annealed) and β annealed wrought material, with the oscillation strategy build behaving more similarly to a β annealed microstructure. The fatigue crack growth rate was lower when cracks were propagated perpendicular to the build layers. For each build strategy, a greater microstructural influence on crack growth rate was found at lower levels of stress intensity factor range (<25 MPa $m^{1/2}$). However, the anisotropy and scatter in the data was much more significant in the case of the oscillation build. These differences have been attributed to the stronger α microtexture heterogeneity present in the oscillation build, which led to a greater crack deflection and bifurcation, giving rise to lower crack growth rates and a higher sensitivity to the anisotropy caused by the directional β grain structure.

1. Introduction

The Titanium alloy Ti–6Al–4V (Ti64) is known for its high static and fatigue strength, fracture toughness, and outstanding corrosion resistance. This excellent combination of mechanical properties has led to its wide-scale application in heavily loaded and safety-critical structures in the aerospace and energy sectors [1]. Because of the high demand and high manufacturing costs involved in producing structural components from titanium alloys, numerous efforts have been made to find potential lower-cost manufacturing routes for producing Ti64 components without compromising their mechanical properties. Additive manufacturing (AM) is a rapidly advancing alternative manufacturing process that offers greater flexibility in producing nearer-to-net shape structural parts, with shorter lead times and much reduced tooling and machining requirements. This can substantially reduce cost in low volume production scenarios [2,3]. However, for aerospace applications, where damage tolerant is important, the performance of the material produced by any new AM technology must still be rigorously assessed under cyclic loading. Significant efforts have been made to understand process-microstructure-property relationships in AM built Ti64 [4–7]. AM process produced microstructures and textures are considerably different to those seen in conventional wrought products, which can affect their mechanical performance [4]. For example, the high cooling rates in AM generally produces a fine lamellar α multi-variant (basketweave) microstructure, which transforms from a relatively coarse β grain structure that develops during solidification. In contrast, forged materials tend to have a coarser α transformation structure, produced by slower cooling rates during heat treatment, consisting of single variant α colonies [4]. Furthermore, specific features of microstructure heterogeneity and crystallographic texture anisotropy

* Corresponding author.
** Corresponding author.
E-mail addresses: abdul.syed@coventry.ac.uk (A.K. Syed), xiang.zhang@coventry.ac.uk (X. Zhang).

https://doi.org/10.1016/j.msea.2021.141194
Received 31 January 2021; Received in revised form 21 March 2021; Accepted 27 March 2021
Available online 3 April 2021
0921-5093/© 2021 The Author(s). Published by Elsevier B.V. This is an open access article under the CC BY license (http://creativecommons.org/licenses/by/4.0/).

inherent to the layer-wise deposition with Ti64 can cause anisotropic fatigue crack growth rates in AM components [8–14].

Wire + Arc Additive Manufacturing (WAAM) technology is a directed energy deposition (DED) process where a wire is fed into a plasma arc heat source at a constant rate to build near-net-shape parts. Due to its high deposition rate and the high-density of material deposition, WAAM has found applications in a range of industries for producing larger-scale (>1 m) metal parts at a more affordable cost, compared to powder-based technologies [15]. However, similar to in other AM processes, the melt pool thermal condition and low solute partitioning in WAAM Ti64 result in coarse columnar primary β grain structures aligned along the material build direction [16–18]. As a consequence, anisotropic tensile properties are frequently measured [16,19]. The larger thermal field and greater layer height also lead to more pronounced Heat Affect Zone (HAZ) banding than is typicality seen in other AM processes [20–22]. Similar studies on other wire-based DED processes have also reported anisotropic tensile properties [23–25].

The high cycle fatigue (HCF) life of simple single pass WAAM wall samples were first measured by Wang et al. [16], at a maximum applied stress of 600 MPa with a cyclic stress ratio of 0.1, in two sample orientations; i.e. with the loading axis either parallel or perpendicular to the deposited layers. This work suggested that the fatigue life was 10% higher than that of standard baseline data [16] for a wrought material in a mill-annealed (i.e. fully recrystallized with no secondary lamellar α) condition. More recently, Biswal et al. [18] have investigated the effect of purposely introduced porosity defects on the fatigue performance of WAAM Ti64 samples with the loading axis perpendicular to the build layers. In this work, the fatigue strength (maximum applied stress at 10^6 cycles) was reduced by 8% in samples with defect sizes smaller than 100 μm and further reduced by around 40% when the defect size was larger than 100 μm. The large scatter found in the test data was shown to be primarily due to the defect location and size. However, a recent follow-up study has revealed that variations in the local microstructure and microtexture around porosity defects can also play an important role in increasing the dispersion in fatigue test data. For example, for the same applied stress, samples with smaller colony size and higher Schmid factor distribution for the pyramidal slip system around the defect had a longer fatigue life [26].

The growth rate of long fatigue cracks has also been investigated by Zhang et al. [27–31], again in simple single pass deposition WAAM Ti64 samples, which were tested at a cyclic load ratio of R = 0.1, with the crack oriented either parallel or perpendicular to the build layers. Both sample orientations showed surprisingly similar crack growth rates [27]. In contrast, Xie et al. [29] showed a 5% lower growth rate when the crack plane was orientated parallel to the build layers, compared to when cracks were orientated perpendicular to the layers. According to Ref. [29], the greater crack deflection was seen when crack crossed the vertical (ND) columnar β grain boundaries, which was the source of lower growth rates parallel to the deposited layers. Further studies reported in Refs. [30,31] have claimed that crack propagation in WAAM Ti64 samples can have a more tortuous crack path, giving a lower crack growth rate than a fully recrystallized (mill annealed) wrought material, where a straighter crack path was found. However, a direct comparison has not yet been made with a wrought β annealed microstructures, where much lower crack growth rates and irregular crack paths are expected [32].

To date, the few studies performed on fatigue performance and anisotropy in long crack growth rates in WAAM Ti64 parts seem to be inconclusive [27,29]. Furthermore, this prior work only used simple test samples consisting of single pass deposition walls, which limited the maximum sample thickness to 9 mm. New deposition strategies have recently been developed for the WAAM process to increase the deposition rate and produce parts with greater and variable wall thickness [33,34], which are closer to practical application. However, to date there has been no accompanying fatigue crack growth test data reported in the open literature for Ti64. A thorough understanding of the influence of such new deposition strategies on the microstructure and fatigue crack growth behaviour of WAAM builds is necessary to support damage tolerant design. This paper, therefore, focuses on comparing the influence of three different deposition strategies used in the WAAM process with Ti64 on the fatigue crack growth behaviour in the as-built condition. The differences in crack growth rates observed are discussed in the context of the different build strategies and their microstructure.

2. Materials and experimental methods

2.1. WAAM Ti64 sample manufacturing process

WAAM Ti64 walls were deposited on a 12 mm thick forged Ti64 substrate using a 1.2 mm diameter wire of grade-5 Ti64, with a plasma arc as the energy source. Three straight wall test samples were built using the three build strategies shown in Fig. 1 (a): i) *'single pass'*: the previously employed single pass wide deposition, used as a baseline, [15]; ii) a *'parallel build'*, built with four parallel passes in each layer aligned with the wall length (WD), and iii)*'oscillation build'*, produced with the process head oscillated across the wall width in TD, while being translated more slowly in WD. During the parallel build (ii), the four tracks were deposited consecutively across the wall width, with a 50% overlap between passes. For each track, the process head was translated in the same direction along the wall. For the oscillation build, the plasma torch and the wire feeder were continuously oscillated across the wall thickness direction (TD), again with an approximate 50% overlap between the melt tracks as the process head was progressively translated along the wall direction (WD). Compared to the parallel build strategy, the oscillation strategy has the advantage of being capable of building parts with continuously varying thickness without altering the process parameters.

One wall was deposited for each build strategy with dimensions in length (L) × height (h) × thickness (t) of; 500 × 120 × 8.5 mm for the *single pass* and 440 × 140 × 22 mm for the *parallel* and *oscillation* builds. After deposition, the walls were cut from the substrate plate and used to extract 5 mm thick C(T) samples, as shown in Fig. 1c–d. The crack growth test samples are distinguished as either "horizontal" or "vertical", as defined in Fig. 1c, with the crack plane orientated in the plane of the layers (WD-TD) or in the ND-TD plane in the build direction, respectively. Four C(T) samples were extracted from the single pass deposition wall, two for each crack orientation. For the parallel pass and oscillation build, five C(T) samples were extracted, two horizontal and three vertical. The C(T) sample geometry and dimensions were specified according to the ASTM E647 standard [35]. For the single pass build (8.5 mm thick), both sides of the wall were first skimmed using high precision milling to reduce the thickness to 5 mm for the C(T) samples. For the parallel and oscillation builds, C(T) samples were extracted directly from the mid-thickness of the wall using wire electric discharge machining (EDM).

2.2. Microstructure and fractography analysis

Samples for microstructural analysis were cut from the WD-ND and TD-ND planes (Fig. 1b) and prepared with standard metallographic procedures; including mounting, grinding with SiC paper, down to 2500 grit size, and polishing using diamond suspension to a 1 μm finish, followed by final polishing with colloidal silica with a 0.02 μm particle size. The samples were then etched with Kroll's reagent for microstructure analysis using an Optical microscope. Scanning electron microscopy (SEM) was used for higher resolution microstructure characterization. For α lath width measurements, cross-section samples were extracted from the WD-ND planes at the midpoint of each wall. Backscatter SEM images taken from these samples were used to measure the average α lath linear intercept width in each build, according to ASTM E1382 standard [36], using the procedure described in detail in Ref. [37]. The length of the intercepts across each line was determined using the

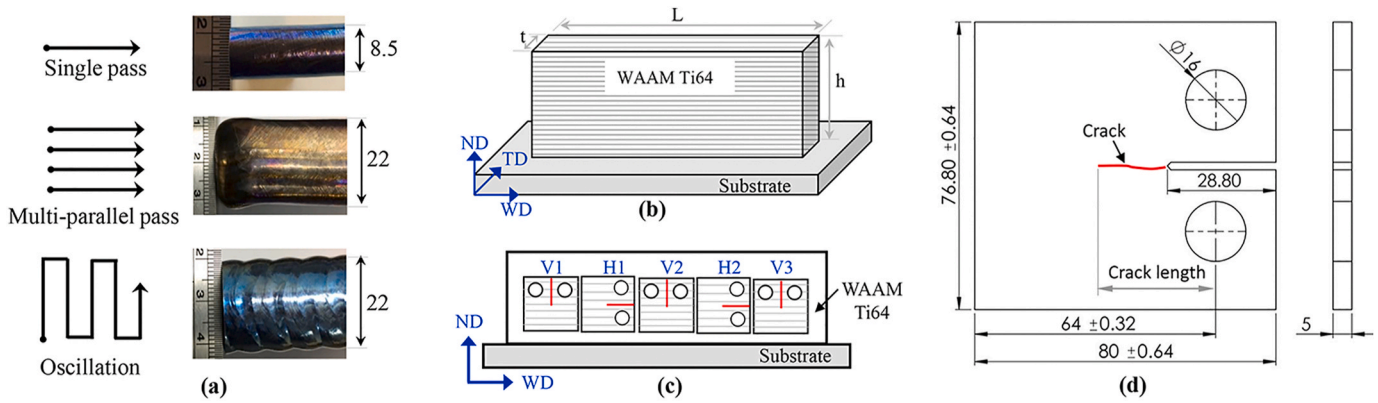

Fig. 1. Schematic diagrams of (a) the deposition strategies, showing accompanying images of the wall top section and thickness, (b) the WAAM Ti64 wall reference frame built with three different deposition strategies, WD = parallel to the wall, TD = the wall transverse or thickness direction, ND = the build height direction; (c) the extraction plan used for the compact tension samples for fatigue testing, showing the samples machined with vertical (V) and horizontal (H) crack orientations. (d) The fatigue crack growth sample, with dimensions in mm.

Image-J software. After crack growth testing, etched fractured samples were used for crack path studies using an optical microscope. In addition, SEM and electron backscattered diffraction (EBSD) was also employed to study the fracture morphology and crack path on unetched samples respectively.

2.3. Fatigue crack growth testing

For each build strategy, two samples were tested in the horizontal crack orientation. In the vertical crack orientation, two samples were tested for single pass and three each for the parallel pass and oscillation build strategies. Constant amplitude load fatigue crack growth tests were carried out at room temperature with a maximum load of 3 kN, using a standard sinusoidal waveform, at a cyclic load ratio of $R = 0.1$ and frequency of 10 Hz. Prior to testing, the anticipated crack path was polished to improve the crack visibility. The crack length was measured by a travelling microscope with 7 × objective magnification and accuracy of ±0.01 mm and averaged between both sides of the sample. Pre-cracking was carried out with a standard load shedding procedure to provide a sharpened fatigue crack of adequate size and eliminate any machined starter notch effects [35]. All samples were pre-cracked to 1 mm before starting the tests. The crack lengths were measured from a distance between the crack tip and the load line centre, as shown in Fig. 1d. The fatigue crack growth rate was deduced from the crack length vs. the number of load cycles using the incremental 7-point polynomial method recommended by ASTM E647 [35]. The relationship of fatigue crack growth rate (da/dN) to the stress intensity factor range (ΔK) was obtained by calculating ΔK from the average crack length using the equations provided in ASTM E647 [35].

3. Results and discussion

3.1. Microstructure

The large-scale microstructural features produced in the WAAM builds due to the translated heat source and layer-wise deposition process can be seen in the optical TD-ND plane macrographs presented in Fig. 2. Different microstructural banding is evident in the etched optical macro-images from the three samples as a result of the different build strategies (highlighted with arrows in Fig. 2). These microstructural bands correspond to heat affected zone (HAZ) produced by the thermal gradient locus up to the β transus temperature, generated by the translated heat source [38–40]. In this transverse (ND-TD) cross-section view, the HAZ bands appear as regularly spaced horizontal lines in the single pass and oscillation build. They exhibit a 'fish scale' like curved pattern in the parallel build. In the parallel build, the curved HAZ bands are formed as the result of viewing end-on the four single parallel melt tracks deposited consecutively across the wall width in each added layer, which were deposited with a 50% overlap between passes. As each consecutive track was deposited from left to right in Figure 2b, these HAZ bands thus tend to exhibit a curvature that tilts progressively towards the right of the build, due to the overlay of the thermal field from adjacent tracks with each previously deposited bead. The sequence by which the four parallel layers deposited in the parallel pass build are marked in Fig. 2b. It can also be noted that the HAZ bands are characterized by a sharp thin white-etched line below which there is a more

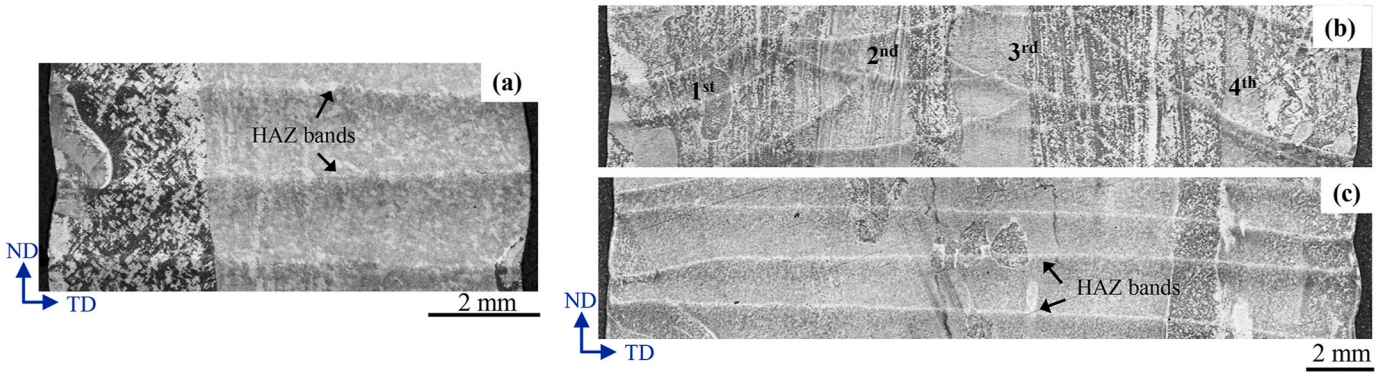

Fig. 2. Large scale optical macro-views of the TD-ND plane showing the HAZ bands in three different builds: (a) single pass, (b) parallel pass, four parallel passes are indicated as 1st, 2nd, 3rd and 4th (c) oscillation build.

progressive darkening of the contrast. This can be seen to repeat in Fig. 2c when each new track is added in the steady-state part of the wall.

The HAZ bands are a characteristic feature of AM processes that are not seen in forged or cast titanium alloys (Fig. 2a–c) but are similar to those observed in Ti64 welds [20]. The bands are caused by re-heating the previously deposited material in the temperature range from about 800 °C to the β transus during subsequent layer deposition [20,21]. This results in both coarsening of the original basketweave lamellar transformation structure within the HAZ bands and appears as dark etched regions. As the temperature increases within the β transus approach curve, thin white etched layers form just below the β transus temperature (~990 °C) which have a finer lamellar spacing and a single variant colony microstructure [21]. In some cases, very fine secondary α can also form within the dark etched layer's upper region [38]. A comprehensive description and analysis of the formation of HAZ bands in AM can be found in Refs. [20,21]. Similar HAZ bands have also been reported in other wire fed [38], powder fed [20] and power bed [39] AM processes. However, the HAZ bands are more pronounced in wire-fed high deposition rate processes due to the higher heat input and greater layer height employed [21].

Further higher magnification WD-ND plane optical micrographs taken from the three build strategies are shown in Fig. 3 to highlight the primary β grain structure. In all three builds, coarse columnar primary β grains can be seen that to have grown across multiple deposited layers, aligned close to the build direction (ND) [37,40,41]. These coarse columnar β grains developed during solidification of WAAM deposits produced in Ti64 are a direct consequence of the steep thermal gradient found at the solidification front in a heated melt pool and the low solute partitioning that occurs in this alloy, which restricts constitutional supercooling [16,42–44]. During the deposition, the translated heat source causes reheating of the previously deposited layers above the β transus temperature, as well as remelting depending on the distance from the heat source. Heating above the β-transus causes the primary β grain structure produced in the previous deposition track to re-grow from the residual β retained in the transformation, reforming the β grain structure below the new fusion boundary of the next melt track. When combined with the low constitutional supercooling possible with Ti64 [16,42,44], this results in solidification primarily by epitaxial growth from the β grains that reform at the fusion boundary and large columnar β grains can therefore continue to develop through multiple deposition layers as each new track is added [45].

Coarse columnar β grain structures are widely reported in other AM processes [10,14,46]. The macrostructure in AM Ti64 is, however, sensitive to the processing conditions. This is evident by the appearance and size of the β grains presented in Fig. 3. The primary β grains are columnar when viewed in the transverse plane in the single pass and parallel pass samples and have lengths cm's in scale that grow through multiple layers. They are also narrower in width than for the oscillation build. The single pass wall has slightly thinner grains than the parallel pass wall owing to the greater buildup of heat during deposition of multiple tracks. The average primary β grain widths in single pass and parallel pass builds were measured as 0.35 ± 0.13 and 0.37 ± 0.18 mm, respectively. In comparison, the columnar grains in the oscillation build were considerably wider with a width of 1.62 ± 0.66 mm. The larger standard deviation in the oscillation build primary β grain widths was due to the smaller number of data points that resulted from the larger grain size which was in the range of 0.4–3.2 mm. In addition, in the oscillation build the optical images also occasionally exhibited smaller primary β grains, which can be observed in Fig. 3c. In the oscillation build, the heat source was rastered across the wall width, leading to a much more rapid heat source return time than when it is translated along the whole length, parallel to the wall. This results in less heat being dissipated before the process head returns and a significantly lower cooling rate, which causes the larger grain size. The rapid reversal of travel direction, and its effect on the preferred growth direction, may also be responsible for forming the smaller primary β grains occasionally seen in the oscillation build.

In AM, the cyclic thermal history that results from the translated heat source and the process parameters (e.g. power, speed, wire feed rate etc.) can have a strong influence on the transformation microstructure. This is strongly affected by the cooling rate below the β transus when it first develops [2], and by the extent of thermal exposure during reheating at temperatures near to, but below the β transus [21]. Fig. 4 shows higher magnification SEM micrographs of the typical transformation microstructure seen between the HAZ bands within the bulk material for the three build strategies. Classical lamellar α+β microstructures, with both Widmanstätten multi-variant (basketweave) and single variant colony morphologies, were found within the primary β grains in all the samples. However, the single pass build had the finest α lath width, followed by the parallel pass, and then the oscillation build which had the coarsest α lamellar structure. The average α lath width (linear intercept) measured for the single pass, parallel pass and oscillation builds were: 0.72 ± 0.16, 0.93 ± 0.13 and 2.32 ± 0.15 μm, respectively. The finest transformation microstructure was found in the single pass build due to its faster cooling rate through the β transus. In comparison, a coarser α lath spacing was seen with the parallel pass build strategy used to produce a wider wall deposit. During parallel pass deposition, four single passes were deposited in parallel to produce each layer and achieve the desired wall width. This not only creates an asymmetry in the thermal field developed due to the pass overlap, but a greater buildup of heat appears to have resulted in a slower cooling rate compared to that experienced in a single pass wide build. The coarsest transformation microstructure was seen with the oscillation build strategy, which was subject to the slowest cooling rate through the $\beta \rightarrow \beta + \alpha$ transformation seen with this particular strategy.

In Fig. 4a, d and f, typical transformation microstructures seen across a β grain boundary are also shown for each build. This provides examples of boundaries with a continuous allotriomorphic layer of grain

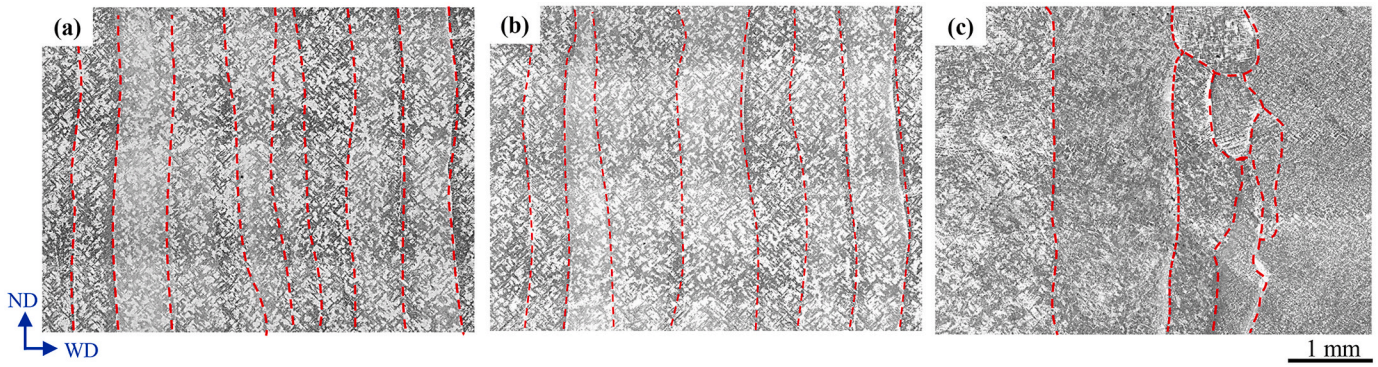

Fig. 3. Wall transvers section optical micrographs (WD-ND plane) showing the columnar primary β grains in the (a) single pass, (b) parallel pass and (c) oscillation builds. The columnar grain boundaries have been delineated.

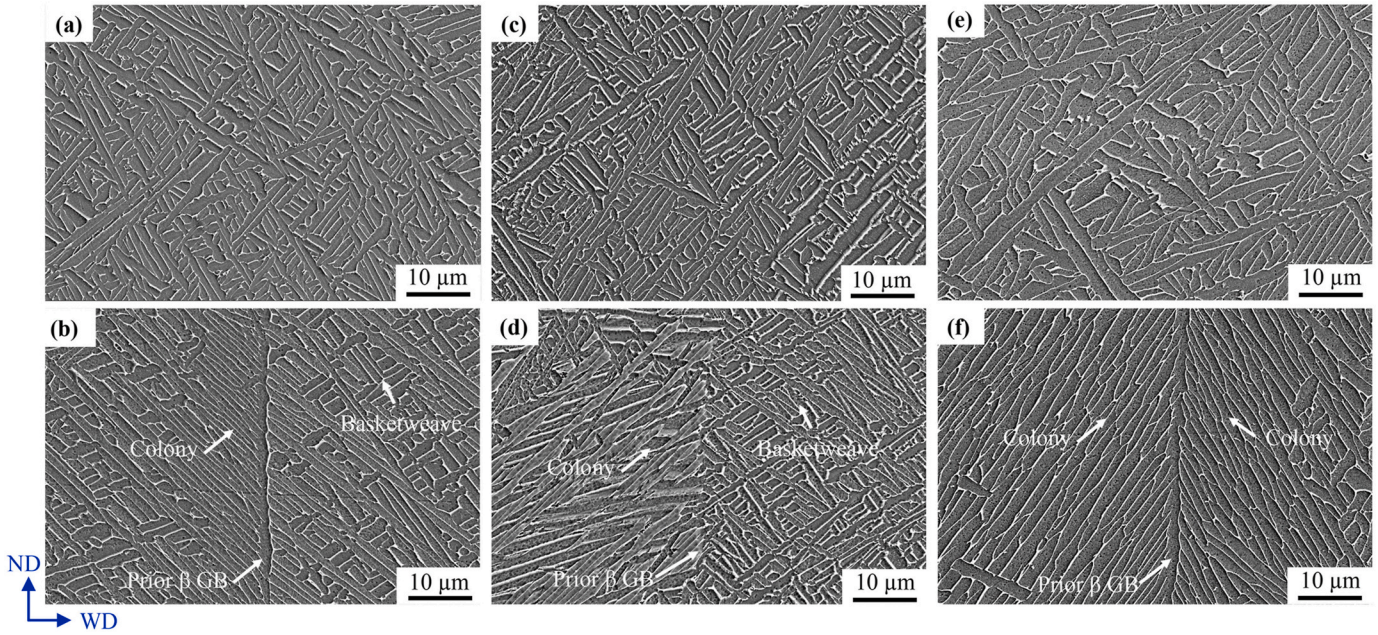

Fig. 4. SEM secondary electron (SE) high magnification images of the typical transformation microstructures found in (a, b) the single pass, (c–d) parallel pass, and (e–f) oscillation builds, showing the microstructure within the center of a β grain and across a β grain boundary for each build strategy.

boundary α (α_{GB}), which nucleated on the prior β grain boundaries, as well as single variant α colonies that have grown from the β grain boundaries into the grains either side. The majority of the β grain boundaries in all the walls had a continuous α_{GB} layer and outward growing single variant α colonies. However, some boundaries (e.g. Fig. 4d) that may have had lower misorientations did not have a well-defined α_{GB} layer. In general, the single variant α colonies extended further into the grains in the oscillation build sample, which again reflects the much lower cooling rate during the β → β + α transformation with this build strategy. In addition, the size of the multi-variant colonies within the β grains were also coarser in the oscillation build sample.

3.2. Fatigue crack growth rates

The fatigue crack growth data obtained for all the horizontal and vertical crack test orientation samples is presented in Fig. 5, as crack growth rate vs. stress intensity factor plots. As a guide and for comparison purposes, the results are also presented along with standard trend lines for the nearest equivalent conventional Ti64 materials, taken from; AMS 4992, for a β annealed casting (10.2 mm thick plate), and β annealed wrought (1050 °C for 1 h and furnace cooled followed by stabilisation annealing at 730 °C for 2 h and furnace cooled; L-T orientation, 10 mm thick), and mill annealed wrought plates (L-T orientation, 6.35 mm thick). Direct comparison with published 'typical' fatigue data should be treated with caution, owing to concerns regarding their reproducibility on different equipment and with different sample widths etc. Nevertheless, overall, for the two parallel build walls (single and multiple tracks wide) at lower ΔK below ~ 12 MPa $m^{1/2}$, the WAAM Ti64 crack growth rate data can be seen to fall below that of the typical mill annealed wrought material, which has a recrystallized fine alpha microstructure, but is above that of a cast or wrought β annealed material, which both have coarse lamellar single α-variant colony microstructures within a coarse β grain structure. This ranking of crack growth rates is expected, given that coarse lamellar single α variant colony microstructures are known to result in greater levels of crack deflection and stronger closure effects in mechanically long cracks, which reduces the effective crack tip ΔK [47]. It is therefore expected that a finer multi-variant basketweave microstructure might fall somewhere between these two extremes. As ΔK increases, it can also be noted that all the data tend to converge as the effects of crack roughness and closure become less important at high ΔK. Although the scatter in the test data is significant between repeated tests, the data for the single pass wall tends to suggest the crack growth rates are slightly higher for the horizontal cracks that grow in WD across the columnar β grain structure and lower in the vertical direction parallel to WD, by a factor of around two at lower ΔK (<20 MPa $m^{1/2}$).

The greater differences in growth rate seen between sample orientations at lower levels of stress intensity are highlighted in Fig. 6, in the ΔK range up to 25 MPa $m^{1/2}$. It can be noted that there is more scatter for the multi-pass parallel build (Figs. 5–6), but again the data suggests that the crack growth rates are slightly lower in the vertical test direction, except for vertical test 3, which seems out of line with the other two. These results thus confirm earlier published findings in Refs. [27,28], where similar single pass builds showed marginal property anisotropy in crack growth rates when ΔK was below 20 MPa $m^{1/2}$, and above this stress intensity, the crack growth was essentially isotropic. Compared to the other tests, the oscillation build samples showed both more scatter and greater anisotropy in their crack growth behaviour. More importantly, lower overall crack growth rates were found in the oscillation build. In the horizontal test orientation, similar results were obtained compared to those for the single pass and parallel pass build strategies that also fell between the baseline comparison curves reproduced from AMS4992 for a typical mill annealed and β annealed wrought material. At low ΔK the crack growth rates were, however, significantly lower in the vertical compared to the horizontal test directions and for two of the three samples this continued to above 20 MPa $m^{1/2}$. Among the three vertical crack samples, vertical test 1 and 3 showed crack growth rates lower by an average of more than 3 × in the vertical crack compared to their horizontal counterparts up to a ΔK of 25 MPa $m^{1/2}$, such that, overall, these samples gave the lowest crack growth rates of all the tests. These growth rate curves also fell below those for all the published reference curves, including that from a β annealed material. However, although vertical test 2 also showed a noticeably lower crack growth rates when ΔK was below 25 MPa $m^{1/2}$, it behaved more similarly to the parallel build tests at high ΔK. The reasons for the greater crack growth anisotropy seen at shorter crack lengths can be related to microstructure differences between samples, which are known to have a stronger

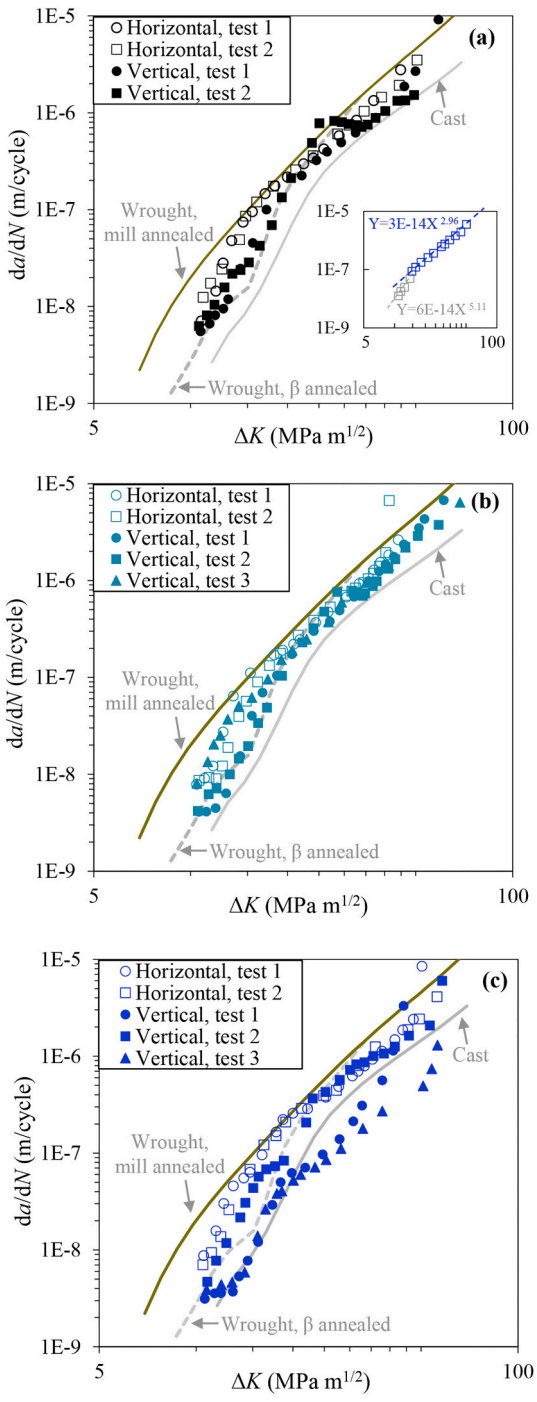

Fig. 5. Crack growth rate vs. stress intensity factor range for (a) single pass, (b) parallel pass, (c) oscillation builds. The inset in (a) shows an example of regression curve fit in two regions to determine the Paris law constants C and m. Curves for conventionally manufactured Ti64 are also shown for comparison purposes; as 'wrought, mill annealed' [48], or 'wrought, β-annealed' [49], and 'as-cast' [48], the later two also have a fully lamella colony α microstructure.

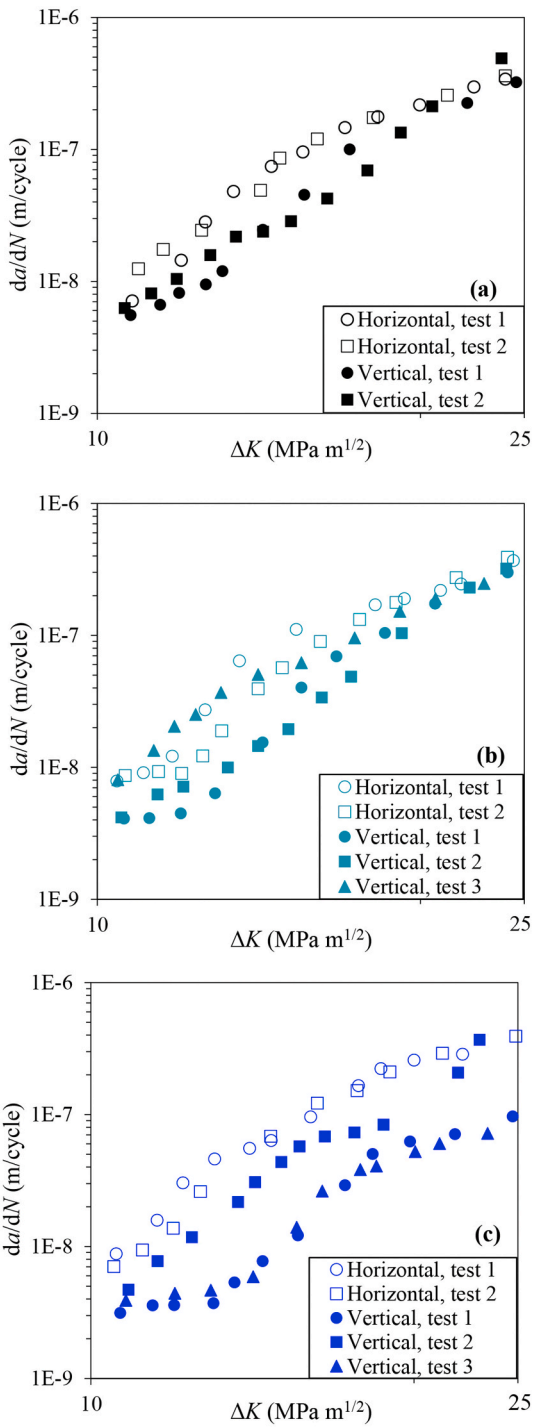

Fig. 6. Enlarged view of crack growth rates in the lower ΔK region up to 25 MPa $m^{1/2}$, to better show the crack growth rate anisotropy between the two crack orientations: (a) single pass, (b) parallel pass, (c) oscillation build.

influence at low ΔK [47,50,51]. The relationships between the differences in the growth rate and the microstructures between the different build strategies will be discussed further below (§3.3). In addition, the presence of HAZ bands consisting of a coarser transformation microstructure [21] might also have influenced the crack growth anisotropy, as the vertical direction cracks propagate predominantly through the matrix of the β grains and rarely encounter the columnar β grain boundaries, but do cross the HAZ bands every layer, which are ~ 1 mm in spacing, and this could potentially lead to crack path deflection locally. In contrast, in the horizontal samples, the cracks encounter no HAZ bands but cross the columnar β grain boundaries at regular intervals equivalent to the grain width, which was smaller than the HAZ band spacing (~0.3 mm).

Generally, the fatigue crack growth rate in metallic alloys is divided into three regions: namely; the threshold region (early stage of fatigue crack growth), the Paris law region (the linear and steady crack growth stage) and the fast growth and final failure stage (unstable/accelerated crack growth stage). The Paris law region is the most useful for

determining damage tolerant design predictions. In this region, the relationship between the crack growth rate and stress intensity factor range is described by Ref. [52]:

$$da/dN = C(\Delta K)^m \quad (1)$$

where, C and m are material constants.

Unlike many conventional metals, where one linear trend curve can be fitted in the Paris law region, Fig. 5 shows two different slopes within the Paris law region; the first segment is between 10^{-8} and 10^{-7} m/cycle (corresponding ΔK range 10–15 MPa $m^{1/2}$), the second is between 10^{-7} to 3×10^{-6} m/cycle (corresponding ΔK range 15–50 MPa $m^{1/2}$) where the crack growth rate curve slope is much steeper than in the first segment. The values of C and m at the two segments have been obtained by the least square curve fitting of the test data in Fig. 5 for the three build strategies (see insert in Fig. 5a). Values of C and m obtained by the regression fit are presented in Table 1. In the lower crack growth rate segment (10^{-8} to 10^{-7} m/cycle), significantly lower C and higher m are found. The difference in the exponent m between the horizontal crack and vertical crack cases in the second segment 10^{-7} to 3×10^{-6} m/cycle is about 15% (2.8–3.4 vs. 3.2–3.5). This means that all the crack growth rate curves in the second segment have a similar slope.

3.3. Crack path and fracture surface analysis

Images of the crack paths developing from the initiation notch are shown in Fig. 7. All the samples showed local crack deflection at quite a short length scale, which is more characteristic of the size of multi-variant colonies found within the coarse β grains. However, a greater influence of the colonies on crack deflection was observed on the fatigue crack growth rate in the oscillation build samples, and the samples built with this strategy also had the lowest crack growth rates (Figs. 5c and 6c). This difference in behaviour can be mainly attributed to two factors. Firstly, the oscillation build strategy resulted in a slower cooling rate, which gave rise to a coarser α transformation structure that contained larger and more defined multi-variant (basketweave) colonies within the β grains, comprised of coarse α lamellae, but also a wider layer of single variant α colonies on the β grain boundaries. Thus, the microtexture variation within this material was both stronger and occurred at a greater length scale than in the single pass and parallel build walls. The oscillation build samples also had lower yield stresses which will increase the plastic zone size. Therefore, in general terms, the transformation microstructure of an oscillation build sample is more similar to that for a β annealed wrought material, and this resulted in greater crack deflection at the scale of the β grain matrix colony size.

Previous studies [53–58] on α/β titanium alloys have also reported lower fatigue crack growth rates in materials with coarse basketweave microstructures due to greater microscopic crack deflection (tortuous crack path [30]). Stronger microtexture variation in the oscillation build also appeared to cause significantly more substantial crack path deflection and bifurcation in the vertical orientation samples, which can change the mode I loading to a mixed mode I and II. This will reduce the mode I crack driving force, thereby reducing the crack growth rate [59]. Such strong crack path deflection effects have also been reported in slowly cooled β annealed lamellar microstructures in heat treated wrought and cast components, but occur far less in recrystallized α microstructures – or mill annealed - wrought material, which has a much smaller α grain size compared to the α colony size in a β annealed material, and this therefore leads to a much lower crack path roughness and higher growth rates [32]. The generally higher yield stress of the WAAM material and shorter slip line length, which is related to the colony size in a lamellar microstructure, or the grain size in a recrystallized α microstructure, will also affect the slip behaviour and plastic zone size at the crack tip.

Overall, the WAAM parallel pass build's crack growth rates probably fall between those of β annealed and mill annealed wrought materials because of differences in both the length scale and strength of crack deflection associated with the multi-valiant colony microstructure prevalent in these materials. For example, the crack profiles presented in Fig. 7 for the oscillation sample showed a rougher crack path, and bifurcation is apparent, involving several secondary cracks growing in parallel to the primary crack resulting in an intense tortuous crack path. Similar to in β annealed wrought materials [32], this would cause a reduction in the effective crack growth driving force of the primary crack and the consequent reduction in the crack growth rate. Finally, more scatter was seen between individual oscillation build vertical test samples, which could be linked to macroscopic crack deflection. For example, test 1 and test 3 showed considerable macroscopic crack path deflection from the beginning of the test, whereas test 2 showed a straighter crack path. After failure, the crack deflection angle was measured as approximately 10° and 13° for test 1 and test 3 respectively. While still complying with the ASTM test standard [35], this crack defection would still cause a reduction in mode I load and contribute to the lower crack growth rate found in these samples.

To further elucidate the origin of the lower crack growth rates and greater fatigue crack path deflection seen in the oscillation build vertical samples, electron backscattered diffraction (EBSD) inverse pole figure maps (coloured with respect to ND) were performed for the vertical samples produced with the three build methods. Fig. 8a–c shows EBSD inverse pole figure maps and schematics of corresponding representation are shown in Fig. 8d–f. In these EBSD maps, the local α orientation colour variation in the basketweave matrix is from multi-variant α colonies that are typically comprised of 3 variants within each colony or microtexture region. In Fig. 8a and b, the crack can be seen propagating through the fine multi-variant α basketweave colonies in the β grain matrix. The higher cooling rates in a single pass and multi-track parallel pass samples had limited deflection as they cross the colony boundaries. In contrast, in the oscillation build sample, both macroscopic crack path and greater local crack deflection can be observed. After the crack initiation just above the primary β grain near the machined notch, the crack is deflected downwards and can be clearly seen to follow a path influenced by the multi-variant (basketweave) α colony microstructure within the coarse β grain present in the map, which makes up the majority of the grains in the oscillation builds. Unlike in a wrought β-annealed material, which has an equiaxed grain structure, the very long columnar β grains will continue to present the same systematic microtexture, maintaining the same 'macroscopic' crack path, until the end of the cm long columnar grain is reached.

A basketweave transformation microstructure consists of a complex interwoven mixture of several repeating α colonies or microtexture regions comprised of different sets of ~3 α orientations, which are subsets [60] of the 12 permissible by the Burgers Orientation Relationship (BOR) within a given parent β grain. Therefore, the crack will tend to grow in a plane favored by the slip systems that can preferentially

Table 1
Paris law constants obtained for the three build strategies at two crack growth rate ranges (averaged from 2/3 test samples).

Build strategy	Sample orientation	Range of da/dN (m/cycle)			
		10^{-8} to 10^{-7}		10^{-7} to 3×10^{-6}	
		C	m	C	m
Single pass build	Horizontal	8.46×10^{-15}	5.92	4.53×10^{-11}	2.83
	Vertical	5.35×10^{-14}	4.93	9.65×10^{-12}	3.22
Parallel pass build	Horizontal	3.33×10^{-15}	6.10	7.70×10^{-12}	3.38
	Vertical	2.14×10^{-13}	4.41	5.79×10^{-12}	3.40
Oscillation pass build	Horizontal	5.92×10^{-15}	6.10	4.43×10^{-11}	2.8
	Vertical	6.58×10^{-11}	2.10	3.44×10^{-11}	3.45

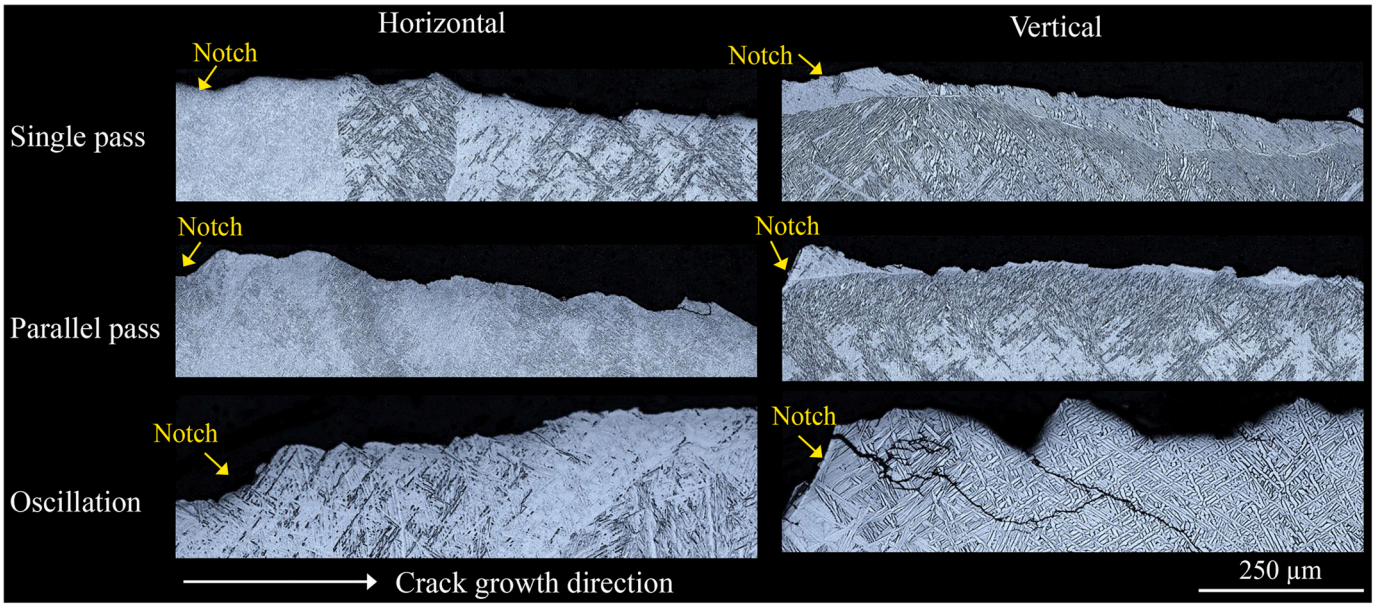

Fig. 7. Macrographs comparing the crack path profiles close to the notch in the horizontal and vertical crack samples.

operate in the set of variants prevalent in each colony, in relation to the crack tip stress field. For example, Pilchak et al. [61] have shown that in single variant colonies in β-annealed material, fatigue cracks prefer to grow parallel to the $\{10\bar{1}0\}$ plane, as this results in symmetric shear stress on two prismatic slip systems at either side of the crack tip. Although it is currently less clear how the more complex microtexture of tri-variant colonies affects the growth of long fatigue cracks in the finer transformation microstructures found in AM, it is apparent that there will still be a preferred plane of propagation that will be active within a range of orientations with respect to applied stress, such that there is a sufficiently high resolved shear stress on the collaborative slip systems involved. Thus, it is not unexpected that the crack will be deflected when it encounters an alternative tri-variant colony within the β grain, as this will generally have a different plane favored for crack propagation.

The interaction of neighboring colonies of 'soft' and 'hard' orientations will cause the crack to change direction with respect to crack growth. This is illustrated in Fig. 8c, where the crack growth direction near the notch is originally determined by the violet-coloured variant ($0\bar{1}11$//ND), which deflects the crack downwards. There can also be an effect of the plate boundaries, with cracks preferring to propagate either parallel to or across the lamellae [61]. This strong association with the crystallographic orientations, or microtexture, of the α variants seen within the multi-variant colonies in the very large β grains that make up the WAAM material will therefore strongly influence the crack path – both in terms of its deflection and micro-roughness. When combined with cracks occasionally being influenced by the different microstructure associated with the β grain boundaries, and their α single variant colonies, this will contribute greatly to scatter in the fatigue crack growth rates, particularly in the near threshold regime [58]. The less strong scatter seen in the crack growth data from the parallel or single pass build strategies is therefore because the basketweave α transformation structure in these materials was considerably finer due to the lower local heat input experienced with these alternative build strategies. This reduced the size of the multi-variant colonies, as well as the size of the packets of variants that made up each colony, which together would be expected to lead to less crack deflection within a β grain and a flatter, more consistent crack surface.

Further investigation of the role of the microtexture is required to explain the much stronger anisotropy seen between the horizontal and vertical growth direction crack growth rates seen in this material and crack path deflection, which requires further work to obtain statistically valid data of the α texture distribution, and this will be the subject of a future publication. Nevertheless, it is apparent that in the horizontal plane the crack will more frequently intercept new β grains, as the columnar grains are relatively narrow in width but cm's long. As the microtexture prevalent in individual grains will be different, this will therefore prevent macroscopic deviation of the crack path from developing as easily when testing in the horizontal directions compared to when a crack propagates parallel to the columnar grain growth direction. In addition, it is known that the β grains have a strong <001>//ND fibre texture in WAAM 'parallel' builds [40,41], which leads to a weaker but significant α transformation texture. It has also been shown that in lamellar microstructures, the α texture can affect crack growth rates [61]. However, in WAAM with a parallel build strategy, the β texture generally has a stronger cube component aligned in ND and WD [40,41], which would be expected to tend to make the transformation texture more symmetric in the vertical and horizontal directions. Therefore, the small anisotropy in the crack growth rates seen in the parallel build samples is probably due to a combination of the crack path roughness variation seen from the β grain structure and texture-related effects.

The overall effect of the different microtexture strengths on the fracture surfaces can be seen in the SEM images in Fig. 9, where at this higher resolution, it can be noted that amongst the three deposition strategies, the single pass and parallel pass builds showed smoother and smaller fracture facets. In contrast, the oscillation build samples clearly have a rougher fracture surface and larger facets. Evidence of anisotropic texturing can also be seen in the macroscopic roughness of the fracture surfaces depicted in Fig. 10, where for the vertical samples an imprint can be observed of the columnar grain structure, where the local texture of the α variants present within each grain biases the preferred crack plane at this length scale. This causes local variation in the inclination of the crack plane in TD across the sample width. In comparison, in the horizontal direction where the crack path would have propagated across the columnar β grains trunks, approximately equiaxed patches of different heights similar to the β grain size can be seen in Fig. 10. In addition, slightly different average roughnesses were measured in the oscillation build for the fracture surfaces with R_a values for the vertical direction being ~10% higher than for the horizontal. However, no evidence was found of the effect of the HAZ bands on this length scale and from these images the crack path roughness was similar in the single and 4 pass parallel builds, which is consistent with the only slightly lower crack growth rate seen in the vertical direction with these samples.

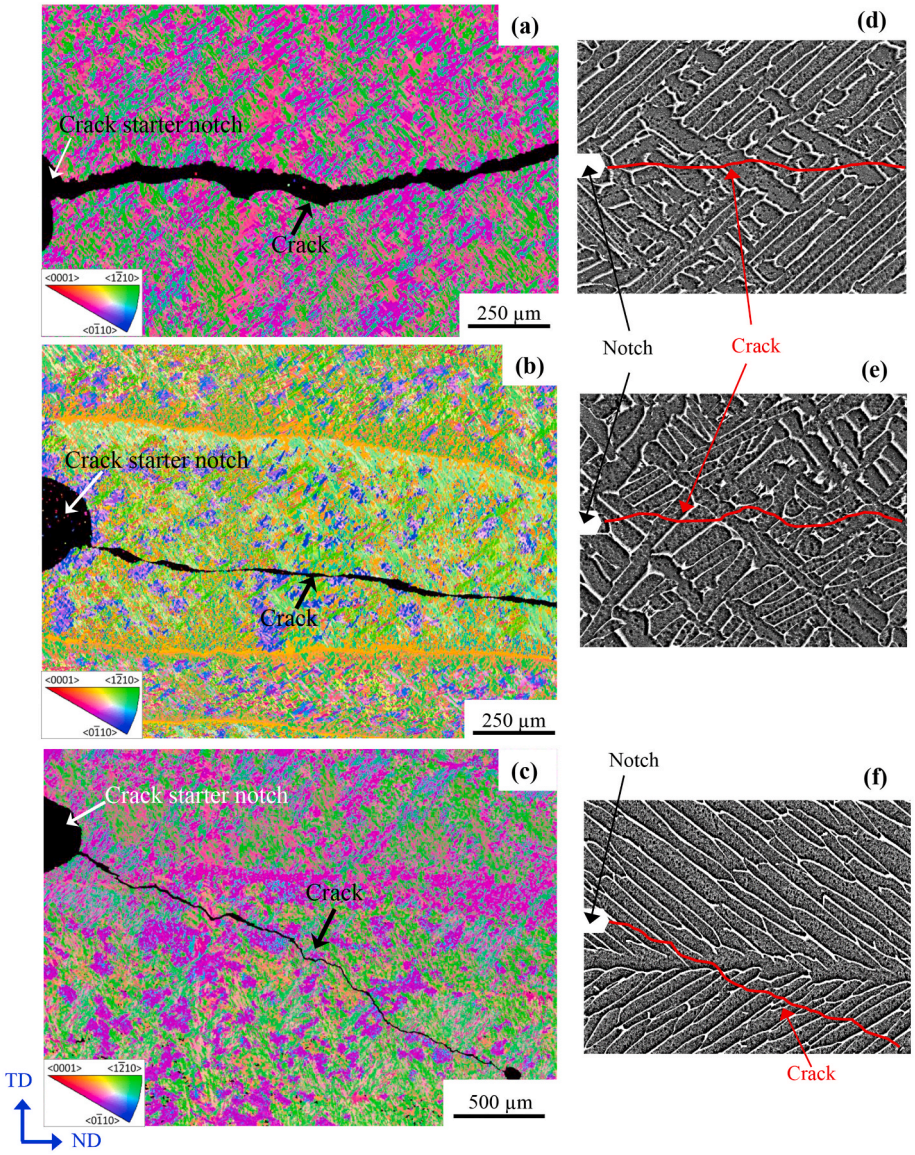

Fig. 8. IPF//ND maps of crack paths in vertical samples of (a) single pass build (b) parallel pass build and (c) oscillation build. Schematics of corresponding representation are shown in (d)–(f).

4. Conclusions

This paper has presented a systematic study of the influence of three different deposition strategies in the WAAM process, i.e. single pass, parallel pass, and oscillation, on the fatigue crack growth behaviour of the alloy Ti64 in the as-deposited condition. Based on the findings, the following conclusions can be drawn.

1. All three build strategies showed the presence of columnar primary β grains being aligned along the material build direction, which is a direct consequence of the epitaxial growth and directional solidification. The oscillation build showed significantly wider columnar β grains and a substantially coarser transformation microstructure consisting of lamellar α multi-variant (basketweave) colonies compared to the single pass and parallel pass builds. In addition, the slower cooling rate in the oscillation build strategy also resulted in wider layers of single variation α colonies on the β grain boundaries.
2. The oscillation build samples were found to have the lowest crack growth rates due to wider layers of single variation α colonies resulting in a more tortuous crack path. In comparison, the finer multi-variant colony microstructure that dominated the single pass and parallel pass build samples led to less crack deflection and higher crack growth rates.
3. Fatigue crack growth rate anisotropy was found for all the build strategies when the stress intensity factor range was below 22–25 MPa $m^{1/2}$. The crack growth rate was lower when cracks propagated perpendicular to the build layers (i.e. parallel to the columnar β grains). However, the anisotropy was relatively small in the case of the higher cooling rate single pass and parallel build samples but much more significant in the oscillation build due to the stronger microtexture heterogeneity and greater crack deflection seen in this material.
4. The difference in α lamellae and colony size were also reflected in the differences in the fracture surfaces with larger facets being seen for the oscillation build and smoother and smaller fracture facets being found for the single pass and parallel pass builds. The vertical samples showed an imprint of higher fracture surface roughness compared to the horizontal samples due to the local texture of the α variants that caused local change in the inclination of the crack plane.

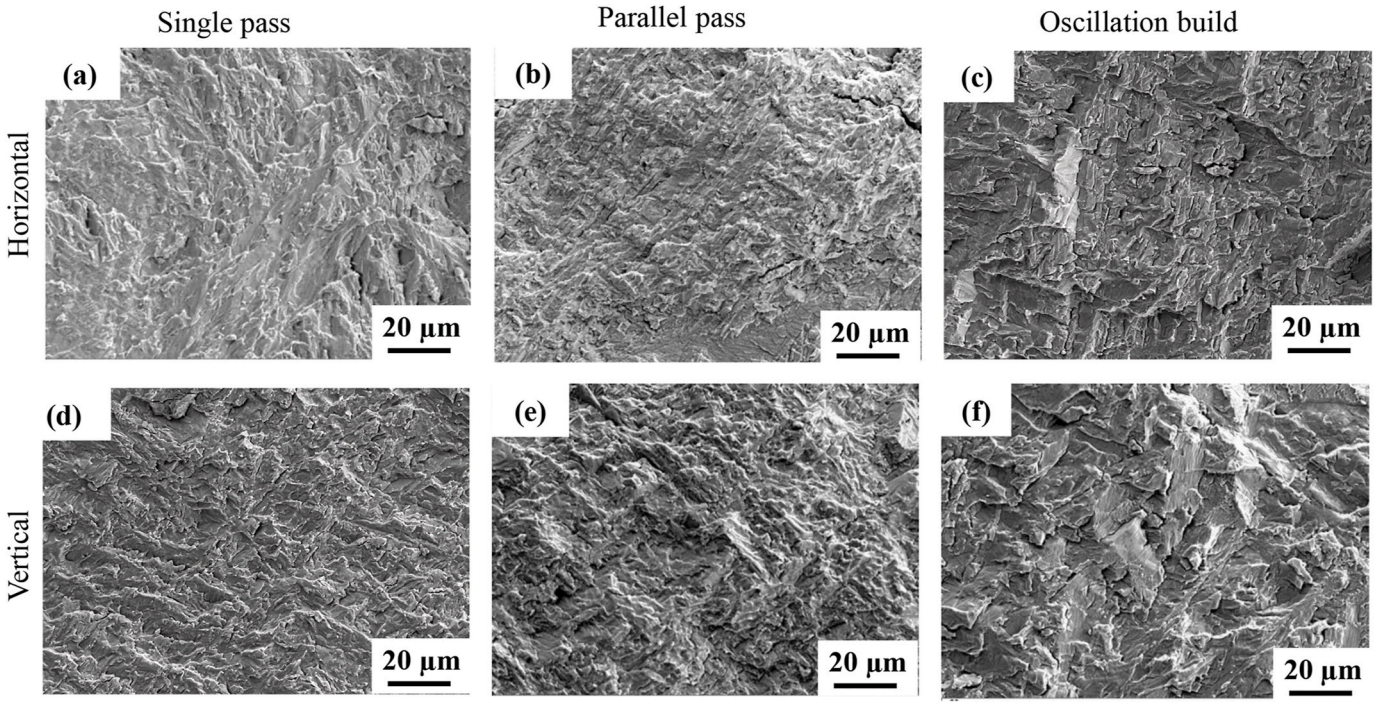

Fig. 9. SEM fracture morphologies of samples taken after failure at approximately 20 mm crack length. (a)–(c) horizontal crack samples, (d)–(f) vertical crack samples.

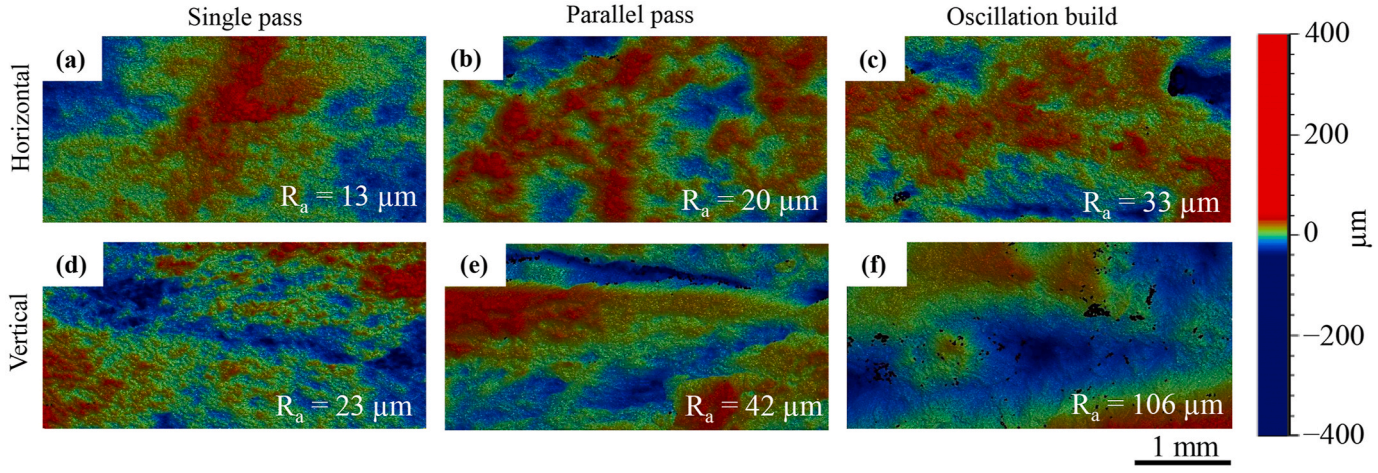

Fig. 10. Fracture surface roughness measured on fractured samples at approximately 20 mm crack length: (a)–(c) horizontal crack samples, (d)–(f) vertical crack samples.

Data availability

The raw/processed data required to reproduce these findings cannot be shared at this time as the data also forms part of an ongoing study.

CRediT authorship contribution statement

Abdul Khadar Syed: Conceptualization, Methodology, Investigation, Formal analysis, Writing – original draft. **Xiang Zhang:** Conceptualization, Methodology, Supervision, Resources, Writing – review & editing, Funding acquisition. **Alec E. Davis:** Investigation, Formal analysis, Writing – review & editing. **Jacob R. Kennedy:** Investigation, Formal analysis, Writing – review & editing. **Filomeno Martina:** Resources. **Jialuo Ding:** Resources. **Stewart Williams:** Resources, Writing – review & editing, Funding acquisition. **Philip B. Prangnell:** Formal analysis, Writing – review & editing, Funding acquisition.

Declaration of competing interest

The authors declare that they have no known competing financial interests or personal relationships that could have appeared to influence the work reported in this paper.

Acknowledgements

We would like to thank Barry Meek, Martyn Cockell and Steve Damms at Coventry University for their support during the sample machining. We also thank the UK Engineering and Physical Science Research Council (EPSRC) for supporting this research through the NEWAM programme grant (EP/R027218/1). Professor P.B. Prangnell is

grateful to the Royal Academy of Engineering, UK, and Airbus for financial support through the Airbus-University of Manchester Centre for Metallurgical Excellence. The authors are also appreciative of the EPSRC programme grant LightForm (EP/R001715/1).

References

[1] C. Cui, B. Hu, L. Zhao, S. Liu, Titanium alloy production technology, market prospects and industry development, Mater. Des. 32 (2011) 1684–1691, https://doi.org/10.1016/j.matdes.2010.09.011.

[2] T. DebRoy, H.L. Wei, J.S. Zuback, T. Mukherjee, J.W. Elmer, J.O. Milewski, A. M. Beese, A. Wilson-Heid, A. De, W. Zhang, Additive manufacturing of metallic components – process, structure and properties, Prog. Mater. Sci. 92 (2018) 112–224, https://doi.org/10.1016/J.PMATSCI.2017.10.001.

[3] W.E. Frazier, Metal additive manufacturing: a review, J. Mater. Eng. Perform. 23 (2014) 1917–1928, https://doi.org/10.1007/s11665-014-0958-z.

[4] S. Liu, Y.C. Shin, Additive manufacturing of Ti6Al4V alloy: a review, Mater. Des. 164 (2019) 107552, https://doi.org/10.1016/J.MATDES.2018.107552.

[5] A. Yadollahi, N. Shamsaei, Additive manufacturing of fatigue resistant materials: challenges and opportunities, Int. J. Fatig. 98 (2017) 14–31, https://doi.org/10.1016/j.ijfatigue.2017.01.001.

[6] C. Körner, Additive manufacturing of metallic components by selective electron beam melting - a review, Int. Mater. Rev. 61 (2016) 361–377, https://doi.org/10.1080/09506608.2016.1176289.

[7] N. Li, S. Huang, G. Zhang, R. Qin, W. Liu, H. Xiong, G. Shi, J. Blackburn, Progress in additive manufacturing on new materials: a review, J. Mater. Sci. Technol. 35 (2019) 242–269, https://doi.org/10.1016/J.JMST.2018.09.002.

[8] V. Cain, L. Thijs, J. Van Humbeeck, B. Van Hooreweder, R. Knutsen, Crack propagation and fracture toughness of Ti6Al4V alloy produced by selective laser melting, Addit. Manuf. 5 (2015) 68–76, https://doi.org/10.1016/j.addma.2014.12.006.

[9] B. Vrancken, V. Cain, R. Knutsen, J. Van Humbeeck, Residual stress via the contour method in compact tension specimens produced via selective laser melting, Scripta Mater. 87 (2014) 29–32, https://doi.org/10.1016/j.scriptamat.2014.05.016.

[10] A.K. Syed, B. Ahmad, H. Guo, T. Machry, D. Eatock, J. Meyer, M.E. Fitzpatrick, X. Zhang, An experimental study of residual stress and direction-dependence of fatigue crack growth behaviour in as-built and stress-relieved selective-laser-melted Ti6Al4V, Mater. Sci. Eng. 755 (2019) 246–257, https://doi.org/10.1016/J.MSEA.2019.04.023.

[11] W. Sun, Y. Ma, W. Huang, W. Zhang, X. Qian, Effects of build direction on tensile and fatigue performance of selective laser melting Ti6Al4V titanium alloy, Int. J. Fatig. 130 (2020) 105260, https://doi.org/10.1016/J.IJFATIGUE.2019.105260.

[12] Y. Zhai, D.A. Lados, E.J. Brown, G.N. Vigilante, Fatigue crack growth behavior and microstructural mechanisms in Ti-6Al-4V manufactured by laser engineered net shaping, Int. J. Fatig. 93 (2016) 51–63, https://doi.org/10.1016/j.ijfatigue.2016.08.009.

[13] C. Li, B. Vrancken, M. Rombouts, J. Van Humbeeck, On the fatigue crack growth performance of Ti6Al4V manufactured by laser metal deposition, in: Proc. 13th World Conf. Titan., John Wiley & Sons, Ltd, 2016, pp. 1453–1457, https://doi.org/10.1002/9781119296126.ch245.

[14] Y. Zhai, H. Galarraga, D.A. Lados, Microstructure, static properties, and fatigue crack growth mechanisms in Ti-6Al-4V fabricated by additive manufacturing: LENS and EBM, Eng. Fail. Anal. 69 (2016) 3–14, https://doi.org/10.1016/j.engfailanal.2016.05.036.

[15] S.W. Williams, F. Martina, A.C. Addison, J. Ding, G. Pardal, P. Colegrove, Wire + Arc Additive manufacturing, Mater. Sci. Technol. 32 (2016) 641–647, https://doi.org/10.1179/1743284715Y.0000000073.

[16] F. Wang, S. Williams, P. Colegrove, A.A. Antonysamy, Microstructure and mechanical properties of wire and arc additive manufactured Ti-6Al-4V, Metall. Mater. Trans. A Phys. Metall. Mater. Sci. 44 (2013) 968–977, https://doi.org/10.1007/s11661-012-1444-6.

[17] B.A. Szost, S. Terzi, F. Martina, D. Boisselier, A. Prytuliak, T. Pirling, M. Hofmann, D.J. Jarvis, A comparative study of additive manufacturing techniques: residual stress and microstructural analysis of CLAD and WAAM printed Ti-6Al-4V components, Mater. Des. 89 (2016) 559–567, https://doi.org/10.1016/j.matdes.2015.09.115.

[18] R. Biswal, X. Zhang, A.K. Syed, M. Awd, J. Ding, F. Walther, S. Williams, Criticality of porosity defects on the fatigue performance of wire + arc additive manufactured titanium alloy, Int. J. Fatig. 122 (2019) 208–217, https://doi.org/10.1016/J.ijfatigue.2019.01.017.

[19] F. Martina, S. Williams, P. Colegrove, Improved microstructure and increased mechanical properties of additive manufacture produced TI-6AL-4V by interpass cold rolling, in: 24th Int. Solid Free. Fabr. Symp. - an Addit. Manuf. Conf., 2013, pp. 490–496. Austin, United States.

[20] S.M. Kelly, S.L. Kampe, Microstructural evolution in laser-deposited multilayer Ti-6Al-4V builds: Part I. Microstructural characterization, Metall. Mater. Trans. 35 (2004) 1861–1867, https://doi.org/10.1007/s11661-004-0094-8.

[21] A. Ho, H. Zhao, J.W. Fellowes, F. Martina, A.E. Davis, P.B. Prangnell, On the origin of microstructural banding in Ti-6Al4V wire-arc based high deposition rate additive manufacturing, Acta Mater. 166 (2019) 306–323, https://doi.org/10.1016/J.actamat.2018.12.038.

[22] A.A. Antonysamy, Microstructure , Texture and Mechanical Property Evolution during Additive Manufacturing of Ti6Al4V Alloy for Aerospace Applications, 2012, p. 316, https://doi.org/10.1007/s11665-013-0658-0.

[23] B. Baufeld, O. Van der Biest, R. Gault, Additive manufacturing of Ti-6Al-4V components by shaped metal deposition: microstructure and mechanical properties, Mater. Des. 31 (2010) S106–S111, https://doi.org/10.1016/j.matdes.2009.11.032.

[24] B. Wu, Z. Pan, D. Ding, D. Cuiuri, H. Li, J. Xu, J. Norrish, A review of the wire arc additive manufacturing of metals: properties, defects and quality improvement, J. Manuf. Process. 35 (2018) 127–139, https://doi.org/10.1016/j.jmapro.2018.08.001.

[25] E. Brandl, F. Palm, V. Michailov, B. Viehweger, C. Leyens, Mechanical properties of additive manufactured titanium (Ti-6Al-4V) blocks deposited by a solid-state laser and wire, Mater. Des. 32 (2011) 4665–4675, https://doi.org/10.1016/j.matdes.2011.06.062.

[26] M. Shamir, A.K. Syed, V. Janik, R. Biswal, X. Zhang, The role of microstructure and local crystallographic orientation near porosity defects on the high cycle fatigue life of an additive manufactured Ti-6Al-4V, Mater. Char. 169 (2020) 110576, https://doi.org/10.1016/j.matchar.2020.110576.

[27] X. Zhang, F. Martina, J. Ding, X. Wang, S.W. Williams, Fracture toughness and fatigue crack growth rate properties in wire + arc additive manufactured Ti-6Al-4V, Fatig. Fract. Eng. Mater. Struct. 40 (2017) 790–803, https://doi.org/10.1111/ffe.12547.

[28] X. Zhang, F. Martina, A.K. Syed, X. Wang, J. Ding, S. Williams, Fatigue crack growth in additive manufactured titanium: residual stress control and life evaluation method development, in: Proc. 29th ICAF Symp., 5-9 June 2017, https://doi.org/10.13140/RG.2.2.29032.16643. Nagoya, Japan.

[29] Y. Xie, M. Gao, F. Wang, C. Zhang, K. Hao, H. Wang, X. Zeng, Anisotropy of fatigue crack growth in wire arc additive manufactured Ti-6Al-4V, Mater. Sci. Eng. 709 (2018) 265–269, https://doi.org/10.1016/J.MSEA.2017.10.064.

[30] J. Zhang, X. Wang, S. Paddea, X. Zhang, Fatigue crack propagation behaviour in wire+arc additive manufactured Ti-6Al-4V: effects of microstructure and residual stress, Mater. Des. 90 (2016) 551–561, https://doi.org/10.1016/j.matdes.2015.10.141.

[31] J. Zhang, X. Zhang, X. Wang, J. Ding, Y. Traore, S. Paddea, S. Williams, Crack path selection at the interface of wrought and wire + arc additive manufactured Ti-6Al-4V, Mater. Des. 104 (2016) 365–375, https://doi.org/10.1016/j.matdes.2016.05.027.

[32] R.K. Nalla, R.O. Ritchie, B.L. Boyce, J.P. Campbell, J.O. Peters, Influence of microstructure on high-cycle fatigue of Ti-6Al-4V: bimodal vs. lamellar structures, Metall. Mater. Trans. 33 (2002) 899–918, https://doi.org/10.1007/s11661-002-0160-z.

[33] H. Lockett, J. Ding, S. Williams, F. Martina, Design for Wire + Arc Additive Manufacture: design rules and build orientation selection, J. Eng. Des. 28 (2017) 568–598, https://doi.org/10.1080/09544828.2017.1365826.

[34] Y. Bandari, T. Charrett, F. Michel, J. Ding, S. Williams, R.P. Tatum, Compensation Strategies for Robotic Motion Errors for Additive Manufacturing (AM), 2016.

[35] ASTM E647-15e1, Standard Test Method for Measurement of Fatigue Crack Growth Rates, ASTM Int., West Conshohocken, PA, 2015.

[36] ASTM E1382-97, standard test methods for determining average grain size using semiautomatic and automatic image analysis, ASTM Int., West Conshohocken, PA, 2015.

[37] F. Martina, P.A. Colegrove, S.W. Williams, J. Meyer, Microstructure of interpass rolled wire + arc additive manufacturing Ti-6Al-4V components, Metall. Mater. Trans. A Phys. Metall. Mater. Sci. 46 (2015) 6103–6118, https://doi.org/10.1007/s11661-015-3172-1.

[38] B. Baufeld, E. Brandl, O. Van Der Biest, Wire based additive layer manufacturing: comparison of microstructure and mechanical properties of Ti-6Al-4V components fabricated by laser-beam deposition and shaped metal deposition, J. Mater. Process. Technol. 211 (2011) 1146–1158, https://doi.org/10.1016/j.jmatprotec.2011.01.018.

[39] S.S. Al-Bermani, M.L. Blackmore, W. Zhang, I. Todd, The origin of microstructural diversity, texture, and mechanical properties in electron beam melted Ti-6Al-4V, Metall. Mater. Trans. A Phys. Metall. Mater. Sci. 41 (2010) 3422–3434, https://doi.org/10.1007/s11661-010-0397-x.

[40] J. Donoghue, A.A. Antonysamy, F. Martina, P.A. Colegrove, S.W. Williams, P. B. Prangnell, The effectiveness of combining rolling deformation with wire–arc additive manufacture on β-grain refinement and texture modification in Ti–6Al–4V, Mater. Char. 114 (2016) 103–114, https://doi.org/10.1016/j.matchar.2016.02.001.

[41] A.A. Antonysamy, J. Meyer, P.B. Prangnell, Effect of build geometry on the β-grain structure and texture in additive manufacture of Ti6Al4V by selective electron beam melting, Mater. Char. 84 (2013) 153–168, https://doi.org/10.1016/j.matchar.2013.07.012.

[42] P. Kobryn, S. Semiatin, Microstructure and texture evolution during solidification processing of Ti–6Al–4V, J. Mater. Process. Technol. 135 (2003) 330–339, https://doi.org/10.1016/S0924-0136(02)00865-8.

[43] M.J. Bermingham, S.D. McDonald, M.S. Dargusch, D.H. StJohn, Grain-refinement mechanisms in titanium alloys, J. Mater. Res. 23 (2008) 97–104, https://doi.org/10.1557/JMR.2008.0002.

[44] M.J. Bermingham, D.H. StJohn, J. Krynen, S. Tedman-Jones, M.S. Dargusch, Promoting the columnar to equiaxed transition and grain refinement of titanium alloys during additive manufacturing, Acta Mater. 168 (2019) 261–274, https://doi.org/10.1016/j.actamat.2019.02.020.

[45] P.A. Colegrove, J. Donoghue, F. Martina, J. Gu, P. Prangnell, J. Hönnige, Application of bulk deformation methods for microstructural and material property improvement and residual stress and distortion control in additively manufactured components, Scripta Mater. 2 (2016), https://doi.org/10.1016/j.scriptamat.2016.10.031.

[46] H. Sharma, D. Parfitt, A.K. Syed, D. Wimpenny, E. Muzangaza, G. Baxter, B. Chen, A critical evaluation of the microstructural gradient along the build direction in electron beam melted Ti-6Al-4V alloy, Mater. Sci. Eng. 744 (2019) 182–194, https://doi.org/10.1016/J.MSEA.2018.12.016.
[47] R.K. Nalla, J.P. Campbell, R.O. Ritchie, Effects of microstructure on mixed-mode, high-cycle fatigue crack-growth thresholds in Ti-6Al-4V alloy, Fatig. Fract. Eng. Mater. Struct. 25 (2002) 587–606, https://doi.org/10.1046/j.1460-2695.2002.00522.x.
[48] Metallic Materials Properties Development and Standardization (MMPDS-04), 2008.
[49] W. Seo, D. Jeong, D. Lee, H. Sung, Y. Kwon, S. Kim, Effects of cooling rate and stabilization annealing on fatigue behavior of β-processed Ti-6Al-4V alloys, Met. Mater. Int. 23 (2017) 648–659, https://doi.org/10.1007/s12540-017-6730-9.
[50] X. Demulsant, J. Mendez, Microstructural effects on small fatigue crack initiation and growth in Ti6Al4V alloys, Fatig. Fract. Eng. Mater. Struct. 18 (1995) 1483–1497, https://doi.org/10.1111/j.1460-2695.1995.tb00870.x.
[51] M. Hassanipour, S. Watanabe, K. Hirayama, H. Toda, K. Uesugi, A. Takeuchi, Effects of 3D microstructural distribution on short crack growth behavior in two bimodal Ti–6Al–4V alloys, Mater. Sci. Eng. 766 (2019) 138264, https://doi.org/10.1016/j.msea.2019.138264.
[52] P. Paris, F. Erdogan, A critical analysis of crack propagation laws, J. Basic Eng. 85 (1963) 528–533.
[53] V. Sinha, W. Soboyejo, An investigation of the effects of colony microstructure on fatigue crack growth in Ti–6Al–4V, Mater. Sci. Eng. 319–321 (2001) 607–612, https://doi.org/10.1016/S0921-5093(01)01014-0.
[54] G.R. Yoder, L.A. Cooley, T.W. Crooker, Fatigue crack propagation resistance of beta-annealed Ti-6AI-4V alloys of differing interstitial oxygen contents, Metall. Trans. A. 9 (1978) 1413–1420, https://doi.org/10.1007/BF02661812.
[55] G.R. Yoder, L.A. Cooley, T.W. Crooker, Quantitative analysis of microstructural effects on fatigue crack growth in widmanstätten Ti-6A1-4V and Ti-8Al-1Mo-1V, Eng. Fract. Mech. 11 (1979) 805–816, https://doi.org/10.1016/0013-7944(79)90138-3.
[56] S. Suresh, Fatigue crack deflection and fracture surface contact: micromechanical models, Metall. Trans. A. 16 (1985) 249–260, https://doi.org/10.1007/BF02815306.
[57] K.S. Ravichandran, Near threshold fatigue crack growth behavior of a titanium alloy: Ti-6A1-4V, Acta Metall. Mater. 39 (1991) 401–410, https://doi.org/10.1016/0956-7151(91)90319-V.
[58] V.K. Saxena, V.M. Radhakrishnan, Effect of phase morphology on fatigue crack growth behavior of α-β titanium alloy-A crack closure rationale, Metall. Mater. Trans. 29 (1998) 245–261, https://doi.org/10.1007/s11661-998-0177-z.
[59] T. Leitner, A. Hohenwarter, W. Ochensberger, R. Pippan, Fatigue crack growth anisotropy in ultrafine-grained iron, Acta Mater. 126 (2017) 154–165, https://doi.org/10.1016/J.ACTAMAT.2016.12.059.
[60] D. Bhattacharyya, G. Viswanathan, R. Denkenberger, D. Furrer, H.L. Fraser, The role of crystallographic and geometrical relationships between α and β phases in an α/β titanium alloy, Acta Mater. 51 (2003) 4679–4691, https://doi.org/10.1016/S1359-6454(03)00179-4.
[61] A.L. Pilchak, R.E.A. Williams, J.C. Williams, Crystallography of fatigue crack initiation and growth in fully lamellar Ti-6Al-4V, Metall. Mater. Trans. 41 (2010) 106–124, https://doi.org/10.1007/s11661-009-0064-2.

https://dspace.org/

Effect of deposition strategies on fatigue crack growth behaviour of wire+ arc additive manufactured titanium alloy Ti-6Al-4V

Syed, Abdul Khadar; Zhang, Xiang; Davis, Alec E.; Kennedy, Jacob R.; Martina, Filomeno ...

2021-04-03
Elsevier
https://doi.org/10.1016/j.msea.2021.141194
Syed AK, Zhang X, Davis AE, et al., (2021) Effect of deposition strategies on fatigue crack growth behaviour of wire+ arc additive manufactured titanium alloy Ti-6Al-4V. Materials Science and Engineering A: Structural Materials: Properties, Microstructures and Processing, Volume 814, May 2021, Article number 141194.

Downloaded from a DSpace repository. https://dspace.org/